1 **New observations of the distribution, morphology, and dissolution dynamics of**

2 **cryogenic gypsum in the Arctic Ocean**

4 **Jutta E. Wollenburg[1*], Morten Iversen[1,2], Christian Katlein[1], Thomas Krumpen[1], Marcel**

5 **Nicolaus[1], Giulia Castellani[1], Ilka Peeken[1], Hauke Flores[1]**

6 [1]Alfred-Wegener-Institut Helmholtz-Zentrum für Polar- und Meeresforschung, D-27570,

7 Bremerhaven, Germany

8 [2]MARUM and University of Bremen, D-27359, Bremen, Germany

9 [*]Corresponding author and requests for materials should be addressed to J.E.W. (email:

10 Jutta.Wollenburg@awi.de)

12   **Abstract**

13   To date observations on a single location indicate that cryogenic gypsum ($Ca[SO_4]\cdot 2H_2O$) may

14   constitute an efficient but hitherto overlooked ballasting mineral enhancing the efficiency of

15   the biological carbon pump in the Arctic Ocean. In June-July 2017 we sampled cryogenic

16   gypsum under pack-ice in the Nansen Basin north of Svalbard using a plankton net mounted

17   on a Remotely Operated Vehicle (ROVnet). Cryogenic gypsum crystals were present at all

18   sampled stations, which suggested a persisting cryogenic gypsum release from melting sea ice

19   throughout the investigated area. This was supported by a sea-ice backtracking model

20   indicating that gypsum release was not related to a specific region of sea ice formation. The

21   observed cryogenic gypsum crystals exhibited a large variability in morphology and size, with

22   the largest crystals exceeding a length of 1 cm. Preservation, temperature and pressure

23   laboratory studies revealed that gypsum dissolution rates accelerated with increasing

24   temperature and pressure, ranging from 6% d^{-1} by mass in Polar Surface Water (-0.5 °C) to

25   81% d^{-1} by mass in Atlantic Water (2.5 °C at 65 bar). When testing the preservation of gypsum

26   in Formaldehyde-fixed samples we observed immediate dissolution. Dissolution at warmer

27   temperatures and through inappropriate preservation media may thus explain why cryogenic

28   gypsum was not observed in scientific samples previously. Direct measurements of gypsum

29   crystal sinking velocities ranged between 200 and 7000 m d^{-1}, suggesting that gypsum-loaded

30   marine aggregates could rapidly sink from the surface to abyssal depths, supporting the

31   hypothesised potential of gypsum as a ballasting mineral in the Arctic Ocean.

33   **Keywords:**

34   Cryogenic gypsum, Arctic Ocean, mineral ballasting, biological carbon pump, sea ice.

35

1   Introduction

Climate change in the Arctic Ocean has led to a drastic reduction of summer sea ice extent as well as to a significant thinning of the sea ice (Kwok, 2018; Kwok and Rothrock, 2009). Sea ice strength has reduced, and increased deformation and fractionation result in a progressively increasing sea ice drift speed (Docquier et al., 2017) and sea-ice export. Over the past decades the ice export via the Fram Strait alone has increased by 11% per decade during the productive spring and summer period (Smedsrud et al., 2017). An increasing amount of sea ice produced in the East Siberian and Laptev Sea melts over the adjacent continental slopes or in the central Arctic Ocean (Krumpen et al., 2019). Overall, the Arctic Ocean sea ice cover has shifted to a predominantly seasonal ice cover. However, although the majority of sea ice diminishes during late summer, the amount of sea ice produced in autumn to winter progressively increases (Kwok, 2018).

Large-scale transformations in the seasonal sea-ice cover impact the physical, chemical and biological dynamics of the sea ice-ocean system. However, especially the interactions of physical-chemical processes within the sea ice and pelagic to benthic biological processes have only received little attention. Of particular importance are poorly soluble minerals precipitated within the brine channels of sea ice which, once released, may ballast organic material sinking to the sea-floor. The changing icescape with more leads and the thinner Arctic sea ice allows increasing light penetration into the under-ice surface water (Katlein et al., 2015; Nicolaus et al., 2013; Nicolaus et al., 2012), supporting fast-growing and often massive under-ice phytoplankton blooms (Arrigo et al., 2012; Arrigo et al., 2014; Assmy et al., 2017). A recent study reported on a sudden export event of an under-ice bloom of the 'unsinkable alga' *Phaeocystis,* caused by the ballasting effect of cryogenic gypsum released from melting sea ice (Wollenburg et al., 2018a). This single event was the first and only report of cryogenic gypsum release in the Arctic Ocean. Moreover, this sea ice precipitation of cryogenic gypsum has never been recorded in Arctic sediments, sediment traps or other field studies.

When sea ice forms, the concentrations of dissolved ions in brine increase, and depending on the temperature of sea ice, a series of minerals (ikaite, mirabilite, hydrohalite, gypsum, hydrohalite, sylvite, $MgCl_2$, Antarcticite) precipitate (Butler, 2016; Butler and Kennedy, 2015; Geilfus et al., 2013; Golden et al., 1998; Wollenburg et al., 2018a). Once released into the ocean, gypsum is considered to be the most stable of the cryogenic precipitates (Butler et al.,

68   2017; Strunz and Nickel, 2001). Sea ice-derived cryogenic gypsum was first described by

69   Geilfus et al. (2013), in a comprehensive work on the chemical, physical, and mineralogical

70   aspects of its precipitation in experimental and natural sea ice off Greenland. According to

71   FREZCHEM, a chemical–thermodynamic model that was developed to quantify aqueous

72   electrolyte properties at sub-zero temperatures, cryogenic gypsum can precipitate at

73   temperatures below −18 °C, and within a small temperature window between −6.5 and −8.5

74   °C (Geilfus et al., 2013; Marion et al., 2010; Wollenburg et al., 2018a). However,

75   measurements on the stoichiometric solubility products showed that gypsum dynamics in ice–

76   brine equilibrium systems strongly depend on the solubility and precipitation of hydrohalite

77   and mirabilite (Butler, 2016; Butler et al., 2017). So far gypsum precipitation in experimental

78   setups were only observed at temperatures between -7.1 and -8.2 °C, and not in the lower

79   temperature range (Butler, 2016; Butler et al., 2017). Moreover, as Arctic sea ice rarely

80   reaches temperatures lower than -18 °C, cryogenic gypsum is more likely precipitated within

81   the higher temperature window in the Arctic Ocean (Wollenburg et al., 2018a).

82   A model applied to understand the gypsum release event of 2015 showed that the ice floe was

83   too warm when it started to form and identified December to February as the most likely time

84   span for gypsum precipitation (Wollenburg et al., 2018a). Due to the absence of a downward

85   brine flux in this advanced phase of sea ice formation, gypsum crystals likely remain trapped

86   in the ice until spring. In the absence of sufficient field observations gypsum release from sea

87   ice is expected to peak at the beginning of the melting season, when sea ice warms to

88   temperatures above -5 °C. This temperature marks the transition in the fluid transport

89   capacities of sea ice allowing brine water and included crystals to be released into the water

90   column (Golden et al., 1998). However, in lack of any extensive, year-round field studies our

91   knowledge depends on models, kinetics and two single field observations (Geilfus et al.,

92   2013; Wollenburg et al., 2018a). There are no studies on sea ice-derived cryogenic gypsum

93   crystal morphologies and its stability in seawater. It is unclear whether gypsum just

94   precipitates during the assumed peak in December to February or whether it continues to

95   grow in remaining brines during sea ice drift.

96   In this study, we systematically investigated the occurrence of cryogenic gypsum release from

97   sea ice in spring 2017 with special emphasis on the morphological properties of the crystals.

98   Varieties of cryogenic gypsum crystal morphologies are described and illustrated. The

99   sampled gypsum crystals were further subjected to various laboratory experiments. Hereby,

100   we investigated the dissolution behaviour over typical depth- and temperature ranges of the

101   Arctic water column and in Formaldehyde solution typically used for biological sampling

102   preservation. We also made direct measurements of the size-specific sinking speed of

103   individual gypsum crystals. These experiments were conducted to answer the question, why

104   cryogenic gypsum has not previously been observed in field studies and if it qualifies as

105   ballast mineral.

106

107

108   **2   Material and Methods**

109   **2.1   Gypsum sampling with the ROVnet and on-board treatment**

110   RV *Polarstern* expedition PS 106 (June-July 2017) in the early melting season gave the

111   opportunity to systematically study the occurrence of cryogenic gypsum release and the

112   morphological properties of gypsum crystals in the area north of Svalbard and on the Barents

113   Sea shelf (Fig. 1A; Table 1).

114   Cryogenic gypsum was sampled from the upper 10 m of the under-ice water at four stations

115   distributed throughout the expedition area (Fig. 1A; Table 1). The first part of the expedition

116   (PS106/1) consisted of a drift study to the north of Svalbard, during which the vessel was

117   anchored to an ice floe (station 32). This ice floe was revisited 6 weeks later at the end of the

118   expedition (PS106/2) (station 80). During the second part of the expedition (PS106/2),

119   cryogenic gypsum was collected over the western Barents Sea (station 45) and in the Nansen

120   Basin to the north-east of Svalbard (station 66).

121   Gypsum crystals were sampled with a plankton net mounted on a remotely operated vehicle

122   (ROVnet, Fig. S1). The ROVnet consists of a Polycarbonate frame with an opening of 40 cm

123   by 60 cm, to which a zooplankton net with a mesh size of 500 μm was attached (Flores,

124   2018). For gypsum sampling, a handmade nylon net with an opening of 10 cm by 15 cm and a

125   mesh size of 30 μm was mounted in the zooplankton net opening. The concentrated

126   particulate material of the small nylon net was collected in a 2 L polyethylene bottle attached

127   to the cod end of the net. A gauze-covered window in the cod-end bottle allowed seawater to

128   drain off. Both nets were mounted on the aft end of a M500 (Ocean Modules, Sweden)

129   observation class ROV carrying an extensive sensor suite described in Katlein et al. (2017).

130 After each ROVnet deployment, the nets were rinsed with ambient sea-water to concentrate

131 the sample in the cod end of the net. The ROVnet sampled horizontal profiles in the water

132 directly below the sea ice. Standard ROVnet profiles were conducted at the ice-water

133 interface, at 5 m and at 10 m depth. The distance covered by each profile ranged between 300

134 and 600 m. At station 32, the 10 m profile was aborted due to technical failure, and at station

135 80 no 5 m profile was sampled due to time constraints, and the subsurface sample was

136 discarded due to handling failure (Table 1).

137 The concentrated particulate material collected in the cod-end bottle of the gypsum sampling

138 net was mixed with a sample equivalent volume of 98% ethanol, and stored at 4 °C until

139 further analyses (Wollenburg et al., 2018a).

140 At ROVnet sampling stations, ice thickness was estimated through thickness drill holes with a

141 tape measure. To characterize the properties of the ice floes sampled on the floe-wide scale,

142 ice thickness surveys were conducted at each sampling station with a GEM2 (Geophex)

143 electromagnetic induction ice-thickness sensor (Katlein et al., 2018).

2.2 Initial analyses of ROVnet samples

145 In the home laboratory the samples were rinsed onto a 32 μm mesh using fresh water. The

146 samples were then oven-dried at 50°C for 20 hours. The remaining crystals were transferred

147 into pre-weighed micropaleontological slides, and their weight was determined with a high-

148 precision Sartorius SE2 ultra-microbalance. Under a Zeiss Axio Zoom V16 microscope,

149 pictures were taken with an Axiocam 506 colour camera. We made both overview images of

150 the whole sample and detailed images of individual crystals. From all samples and crystal

151 morphologies, individual crystals were analysed using Raman microscopy, which confirmed

152 that the crystals were gypsum (Wollenburg et al., 2018a). As in some samples both, very large

153 and very small crystals (Figs. S3-S4) were observed, the >32 μm samples were dry-sieved

154 over a 63 μm analysis sieve. The length and width of the cryogenic gypsum crystals in the

155 size fractions >32<63 μm and >63 μm was determined with the software application ImageJ

156 on 50 crystals in each sample and size fraction (Schneider et al., 2012) (Tab. 2).

2.3 Initial analyses of ice cores

158 At all ice stations, sea ice cores for archive purposes and for further measurement of bottom

159 communities were drilled with a 9 cm diameter ice corer (Kovacs Enterprise) and stored at -

160 20°C (Peeken, 2018). One ice-core from station 80 and four bottom slices (10 cm) of ice-
161 cores from station 45 were studied to investigate the gypsum crystal morphologies within sea
162 ice. Each section was transferred into a measuring jug with lukewarm tap water for approx.
163 two seconds, and then the jug was emptied over a 32 μm analysis sieve, and repeatedly
164 refilled. This process was continued until all ice was melted. With the aid of a hand shower
165 and a wash bottle the residue on the sieve was rinsed and transferred into a 30 μm mesh-
166 covered funnel, dried and transferred into a micropaleontological picking tray for inspection
167 and documentation. For storage, the residue was transferred into pre-weighed labelled
168 micropaleontological slides.

2.4   Dissolution experiments

The aim of our dissolution experiments was to investigate the persistence of gypsum crystals
against dissolution in the Arctic water column (water mass trials) and under common
biological sample treatment (Formaldehyde trial).

Dissolution experiments were carried out on individual gypsum crystals collected from
ROVnet samples. Hereby, 5 cryogenic gypsum crystals with different crystal morphologies,
and from both size fractions were used in each reaction chamber. Before the start and after the
termination of each experiment, pictures of the cryogenic gypsum crystals used were taken
with an Axiocam 506 colour camera under a Zeiss Axio Zoom V16 microscope. The weight
of the crystals before and after each treatment was determined with a high-precision Sartorius
SE2 ultra-microbalance after they had been transferred into a pre-weighted silver boat. The
experimental running time of each experiment was 24 hours.

2.4.1   Water mass trials

The experiments to simulate dissolution within the different water masses and hydrostatic
pressure regimes of the Arctic Ocean were carried out with high-pressure chambers installed
in a cooling table (Wollenburg et al., 2018b). With a high-pressure pump (ProStar218 Agilent
Technologies), peak tubing, and multiple titanium valves a continuous isobaric and isocratic
one-way seawater flow of 0.3 ml/min was directed through a set of four serially arranged
high-pressure chambers each with an internal volume of 0.258 ml (Wollenburg et al., 2018b).
This setup allowed for dissolution experiments at defined pressures and temperatures
(Wollenburg et al., 2018b). For the experiments, we used sterile-filtered (0.2 μm mesh) North
Sea water that was adjusted to a salinity of 34.98 by addition of 1 g Instant Ocean® sea salt

191 per L and psu-offset. The natural pH of 8.1 after equilibration to the refrigerator's atmosphere

192 (at 2.5 °C and at atmospheric pressure), lowers to pH 8.05 at 2.5 °C at 150 bar (Culberson and

193 Pytkowicx, 1968). Five experiments, with 4 high-pressure chambers were carried out. The

194 Polar Surface (PSW) water corresponding experimental trial was running at -0.5 °C and 3 bar,

195 the experimental Atlantic Water (AW) trial at +2.5 °C and 65 bar, and three experimental

196 Deep Water trials were conducted at -1 °C and 100, 120 and 150 bar, respectively.

197 **2.4.2   Formaldehyde trial**

198 To study the effect of Formaldehyde treatment on cryogenic gypsum, the crystals were

199 subjected to a Formaldehyde solution of 4% in seawater, which is commonly used to preserve

200 biological samples. The stock solution consisted of 500 ml Formaldehyde concentration of

201 40%, 500 ml aqua dest. and 100 g hexamethylenetetramine, adjusted to a pH of 7.3-7.9.

202 Aliquots of the 20% stock solution were added to the four-fold volume of artificial Arctic

203 Ocean sea water to obtain a final concentration of 4%.

204 The Gypsum crystals were transferred into Falcon Tubes, and the 4% Formaldehyde solution

205 was added. The Falcon tubes were then either stored at 3 °C, or at room temperature. After

206 the experiments, the gypsum crystal-Formaldehyde suspension was washed with deionized

207 water over a 10 μm mesh using a wash bottle, and dried on gauze. As in all formaldehyde

208 trials all gypsum dissolved, no post-experimental weight was determined.

209

210 **2.5   Size-specific settling velocities of gypsum**

211

212 The size-specific sinking velocity of cryogenic gypsum was measured in a settling cylinder

213 (Ploug et al., 2008). The cylinder (30 cm high and 5 cm in diameter) was filled with filtered

214 seawater (salinity 32) and surrounded by a water jacket for thermal stabilization at 2 °C. The

215 settling cylinder was closed at both ends, only allowing insertion of a wide-bore pipette at the

216 top. Immediately before measurement, the gypsum was submerged into seawater with a

217 salinity of 32 and a temperature of 2 °C, and then transferred to the settling cylinder with a

218 wide-bore pipette. The gypsum crystals were allowed to sink out of the wide-bore pipette,

219 which was centered in the cylinder. The descent of the crystals was recorded by a Basler 4

220 MPixel Ethernet camera equipped with a 25 mm fixed focal lens (Edmund Optics). The

221 settling column was illuminated from the sides by a custom-made LED light source. The

222 camera recorded 7 images per second as the gypsum crystals sank through the settling

223 column. The setup was calibrated by recording a length scale before sinking velocity

224 measurements. The size and settling of the individual gypsum crystals was determined with

225 the image analysis software ImageJ. This was done by using the projected area of the crystals

226 to calculate the equivalent spherical diameter and the distance traveled between the

227 subsequent images to determine the sinking velocity of the individual crystals (Iversen et al.,

228 2010)

229

230 **2.6   Backtracking the sampled ice flows under which cryogenic gypsum was sampled**

231

232 To determine sea ice drift trajectories of sampled sea ice we used a Lagrangian approach

233 (IceTrack) that traces sea ice backward or forward in time using a combination of satellite-

234 derived low resolution drift products. So far, IceTrack has been used in a number of

235 publications to examine sea ice sources, pathways, thickness changes and atmospheric

236 processes acting on the ice cover (Damm et al., 2018; Krumpen et al., 2016; Peeken et al.,

237 2018). A detailed description is provided in Krumpen et al. (2019).

238 Sea ice motion information was provided by different institutions, obtained from different

239 sensors, and for different time intervals. In this study we applied a combination of three

240 different products: (i) motion estimates based on a combination of scatterometer and

241 radiometer data provided by the Center for Satellite Exploitation and Research (CERSAT

242 (Girard-Ardhuin and Ezraty, 2012), (ii) the OSI-405-c motion product from the Ocean and

243 Sea Ice Satellite Application Facility (OSISAF (Lavergne, 2016), and (iii) Polar Pathfinder

244 Daily Motion Vectors from the National Snow and Ice Data Center (NSIDC (Tschudi et al.,

245 2016).

246 The tracking approach works as follows: An ice parcel is traced backward or forward in time

247 on a daily basis. Tracking is stopped if a) ice hits the coastline or fast ice edge, or b) ice

248 concentration at a specific location drops below 50% and we assume the ice to be formed or

249 melted. The applied sea ice concentration product was provided by CERSAT and was based

250 on 85 GHz SSM/I brightness temperatures, using the ARTIST Sea Ice (ASI) algorithm.

251

252 **3   Results**

253 **3.1   Presence and distribution of cryogenic gypsum under the investigated ice-floes**

254 Based on backtracking (Krumpen, 2018) and sea ice observations, the sampled ice-floes had

255 an age of 1 to 3 years (Fig. 1B) and were originating from the Siberian Sea (station 32/80), the

256 Laptev Sea (station 45), and were more locally grown in the Nansen Basin (station 66).

257 Whereas the mean sea ice thickness at the ROV survey stations ranged between 94 and 156

258 cm, the mean sea ice thickness of the investigated ice-floes estimated by an ice-thickness

259 sensor surveys (Katlein et al., 2018) was 1.90 m for station 32, 1.00 m for station 45, and 1.80

260 m for stations 66 and 80 (Fig. 1A, Table 1). Despite the different origins and thicknesses of

261 sea ice, cryogenic gypsum crystals were found at all stations and in all depth layers sampled

262 with the ROVnet (Figs. 1A, B, Tab. 1). At all stations and sampling depths the samples were

263 dominated by cryogenic gypsum, with a proportional dry weight of >96.5% in the 5 m-sample

264 at station 32, and with >99% in all other samples (Figs. 2, Figs. S2-S5). Other lithogenic

265 particles, as often found in sea ice (Nürnberg et al., 1994), were essentially absent.

266 **3.2   The morphology of cryogenic gypsum**

267 The samples collected at station 32 were dominated by rounded, matte, solid cryogenic

268 gypsum crystals with a mean length-width ratio of 1.40-1.76 (Tab. 2, S2). The proportional

269 mass contribution of the smaller-sized crystals of the >30<63 μm size fraction increased with

270 depth and outweighed the contribution of the >63 μm size fraction with 56.30%, and 66.28%

271 for the 0 and 5 m water depth sample, respectively (Fig. 3). At 0 m, the mean length of the

272 crystals was 68.46 μm in the >63 μm size fraction and 44.27 μm in the >30<63 μm fraction.

273 At 5 m depth, crystal dimensions were similar, ranging at mean crystal lengths of 63.28 μm in

274 the >63 μm, and 35.90 μm in the >30<63 μm size fraction, respectively.

275 At station 45, the crystals were mostly solid and for most part hyaline, rather than matte

276 crystals as at station 32 (Figs. 2C-D, 6, S3). With decreasing weight proportion, the >63 μm

277 size clearly dominated the 0, 5, and 10 m samples with 79.90, 73.39, and 66.14%,

278 respectively. In the 0 m layer samples, mean crystal lengths were 114.18 μm in the >63 μm

279 size fraction and 58.74 μm in the >30<63 μm size fraction (Tab. 2). At 5 m depth, we

280 observed mean crystal lengths of 111 μm in the >63 μm size fractions, and 56.73 μm in the

281 >30<63 μm fraction. The mean crystal lengths in the 10 m sample was 92.83 and 50.32 μm

282 for the >63 and >30<63 μm size fraction, respectively. At station 45 the crystal length-width

283 ratio varied between 1.37 and 1.98, measured in the >30<63 μm size fraction of the surface

284 sample, and the >63 μm size fraction of the 10 m sample. The cryogenic gypsum crystals

285 retrieved from the melted ice core drilled at this station were solid and hyaline. In size and

286 shape they resembled the crystals of the 10 m layer at this station, with a mean crystal length

287 of 114.2 μm, mean width of 57.2 μm, and a length-width ratio of 2 (Fig. 4).

288   At station 66, the crystals from 0 m water depth were dominated by large, pencil-like, hyaline

289   and solid crystals with a mean crystal length of 1,355 μm and mean width of 415 μm in the

290   dominating >63 μm fraction (99.25% mass) (Fig. 2B, S4, Tab. 2). These crystals with an

291   average length-width ratio of 3.27 were found as isolated crystals, but very often also as inter-

292   grown crystal rosettes with two to more than 10 individual crystals involved (Fig. S4; Tab. 2).

293   The >30<63 μm size fraction (0.75% mass) was dominated by matte, whitish, rounded

294   gypsum particles and tiny gypsum needles with a mean crystal length of 56.67 μm (Fig. S4,

295   Tab. 2.). As at the other stations the weight proportion of the >63 μm size fraction

296   significantly decreased from 99.25 in the 0 m, to 75.23 at 5 m, and 61.18% in the 10 m

297   sample (Fig. 2). The size of cryogenic gypsum crystals collected from the 5 and 10 m layers

298   was significantly smaller and predominantly composed of isolated small hyaline and euhedral

299   gypsum needles. The length-width ratio ranged between 5.60 (5 m) and 4.37 (10 m) (Figs.

300   2A, S4, Tab. 2). In the 5 m layer sample, the mean crystal length was 411.42 μm in the >63

301   μm size fraction, and 62.03 μm in the >30<63 μm size fraction. The 10 m samples showed a

302   mean crystal length of 101.40 μm in the >63, and 30.71 μm in the >30<63 μm size fraction

303   (Tab. 2).

304   In the 10 m layer sample of station 80, large tabular gypsum crystals measuring up to 1 cm in

305   length (mean length: 3,078 μm, mean width: 1,830 μm) dominated the >63 μm size fraction.

306   Their average length-width ratio was 1.7. This size fraction contributed 89.1% of the gypsum

307   mass (Figs. 5, S5, Tab. 2). The >30<63 μm size fraction was composed of fragments of these

308   large crystals and few small gypsum needles. These often intergrown columnar crystals

309   looked bladed, for most part also dented and with numerous cracks. Their mean length was

310   71.8 μm. The ice core retrieved from this station was very porous and broke into pieces of 9

311   to 11 cm. Cryogenic gypsum was retrieved from all these ice core sections and revealed a

312   dominance of extraordinary large crystals (Figs. 5, S5), resembling the ROVnet samples from

313   this station. The largest cryogenic gypsum crystals >6,000 μm (mean crystal length: 2,821

314   μm, mean width: 1,689 m) were retrieved from the top-most 8 cm ice core section, whereas,

315   the maximum crystal size gradually decreased downcore (Fig. S5). The crystals themselves

316   lacked sharp corners, and the large crystals had cavities inside, indicating an advanced stage

317   of dissolution (Figs. 5C-D; S5).

318

319   **3.3   Dissolution experiments**

3.3.1 Experiments to simulate cryogenic gypsum dissolution within the Arctic water column

Our study area was characterized by the presence of three main water masses (Nikolopoulos et al., 2018; Rudels, 2015): 1) The Polar Surface Water (PSW) including the halocline, with a variable mean salinity of 32 and a temperature range of -1.8 to 0.0 °C, extended from the surface to maximum 100 m water depth (Nikolopoulos et al., 2018). 2) The Atlantic Water (AW) with a mean salinity of 34.4 to 34.7 and variable temperature of 0.0 to 4.7 °C in the study area extended from below the PSW to 600-800 m water depth (Nikolopoulos et al., 2018). 3) The Eurasian Arctic Deep Water (EADW) fills the deep Eurasian Basin below the AW with a temperature range of <0 to -0.94 °C and a salinity of about 34.9 (Nikolopoulos et al., 2018).

The dissolution experiments carried out to simulate dissolution in the PSW were set to 3 bar, -0.5 °C. Over the 24 hours lasting PSW-simulating dissolution experiment, about 6% of the gypsum dissolved (Figs. 6, S6A, Tab. 3). In the AW experiment, the combination of positive temperatures (2.5 °C) and a pressure of 65 bar impacted the dissolution on the cryogenic gypsum crystals more than in any other seawater trial. More than 80% of the cryogenic gypsum crystals dissolved during the 24-hours experiment (Figs. 6, S6B, Tab. 3). Moreover, as dissolution mainly affects the crystal's surface, smaller gypsums crystals and those with increased surface roughness were preferentially impacted by dissolution, whereas larger and solid crystals with smooth surface showed the lowest dissolution (Fig. S6B). The EADW-simulating dissolution experiments set to a temperature of -0.5 °C showed a progressive cryogenic gypsum dissolution of 26, 58, and 62% with increasing pressure for the 100, 120 and 150 bar experiments, respectively (Figs. 6, S7, Tab. 3).

3.3.2 Experiments to simulate cryogenic gypsum dissolution within Formaldehyde-treated biological samples

In the Formaldehyde experiments we exposed our set of cryogenic gypsum crystals to a Formaldehyde solution of 4%, which is commonly used to store pelagic samples from the Polar Oceans (Edler, 1979). Irrespective of the temperature at which the sample was stored, all gypsum dissolved within 24 hours.

3.4 Sinking velocities of gypsum crystals

351 The sinking velocity (*SV*) of the gypsum crystals increased with crystal size (Fig. 7). Small

352 crystals with an equivalent spherical diameter (*ESD*) of 200 μm sank with 300 m d^{-1} while

353 large gypsum crystals with ESDs of 2,000 to 2,500 μm sank with velocities of 5,000 to 7,000

354 m d^{-1}. The size to settling relationship was best described by a power function (SV = 4239.9

355 ESD$^{0.839}$, R^2 = 0.84).

356

357 **4   Discussion**

358

359 **4.1   Distribution and morphology of cryogenic gypsum crystals**

360

361 This study shows for the first time the wide-spread presence of cryogenic gypsum under melting

362 Arctic sea ice of different origin. At all stations cryogenic gypsum dominated the sample

363 fraction of particles >30 μm in Eurasian Basin surface waters, indicating a continuous cryogenic

364 gypsum flux from melting sea ice over a period of six weeks.

365 When designing the ROVnet for cryogenic gypsum sampling, we opted for the coarser >30 μm

366 mesh to prohibit an overflow of the sampling container when running into a phytoplankton

367 bloom. However, as Geilfus et al. (Geilfus et al., 2013) had observed gypsum crystals as small

368 as 10 μm, we probably lost an unknown proportion of smaller gypsum crystals by the chosen

369 sampling strategy. The gypsum crystals described from sea ice so far retrieved from only 3-

370 days-old experimental and 30 cm thick natural sea ice off Greenland were small (crystal length

371 max. 100 μm), planar euhedral gypsum crystals often intergrown or as rosettes (Geilfus et al.,

372 2013). Similar, but larger (crystal length up to 1 mm), gypsum crystals were observed within

373 *Phaeocystis* aggregates collected in the region of the present study (Wollenburg et al., 2018a).

374 However, here we show that gypsum crystals exhibit a strong variability in size and

375 morphology. Particularly large crystals were characterised by more complex shapes (Fig. 2, 5,

376 S3-4) and increased surface roughness (Figs. S7C-D), compared to the small planar euhedral

377 (Fig. 2A) and more spherical crystals (Fig. S7A-B). Euhedral crystal needles larger but

378 otherwise similar to those described by Geilfus et al. (2013) and Wollenburg et al. (2018a)

379 dominated the >63 μm fraction collected at 5 and 10 m depths at station 66, and smaller crystals

380 contributed especially to the >30<63 μm size fraction of the station's subsurface samples.

381 As cryogenic gypsum forms in sea ice brine pockets or channels, the size and morphology

382 especially of large crystals is likely determined by sea ice texture and porosity during gypsum

383   precipitation. Pursuing this hypothesis, the large and intergrown crystals collected from the

384   0 m layer at station 66, and the 10 m layer and ice-core at station 80, formed in highly

385   branched granular sea ice (Lieb-Lappen et al., 2017; Weissenberger et al., 1992). In contrast,

386   the small cryogenic gypsum needles reported by Geilfus et al. (2013) and Wollenburg et al. (

387   2018a), may have preferentially formed in columnar sea ice. Even sampling the same ice-floe

388   (station 32 and 80), the appearance of the crystals changed. Possibly, a widening of the brine

389   channels during the elapsed time (6 weeks) allowed a release of larger crystals at station 80

390   when compared to station 32. However, crystal growth during this elapsed period or lateral

391   advection of large crystals cannot be excluded. Thus, detailed texture analyses on sea ice

392   cores prior to sampling are needed to validate or reject hypotheses on a link between sea ice

393   porosity and cryogenic gypsum crystal size and morphology and should be considered in

394   future studies.

395   The sea ice microstructure dictating the formation of gypsum crystals in the brine matrix

396   likely varied among ice-floes due to different ages, origins and drift trajectories (Fig. 1B). For

397   example, station 66 was the only station where the sea ice likely formed over the central

398   Nansen Basin only months before our study (Fig. 1B). The surface sample of station 66 had

399   large intergrown hyaline star-shaped gypsum crystals that were observed at no other station.

400   They also showed a considerably higher length-width ratio than crystals from second-year ice

401   of stations 32/80 and 45 (Fig. 1B; Fig. 2). Accordingly, a close relationship between local sea

402   ice properties and gypsum crystal morphology in the underlying water was evident from the

403   comparison of gypsum crystals collected with the ROVnet with those retrieved from ice cores

404   collected at two stations. The ice-core samples revealed cryogenic gypsum crystals that

405   basically resembled the crystal morphologies collected from the water column at the same

406   stations, indicating that the gypsum morphologies observed in the water column likely reflect

407   the gypsum precipitation conditions and brine-channel structure of local ice-floes. The current

408   understanding of mineral precipitation in supersaturated brines relies on ice-core analyses, sea

409   ice brine- and experimental studies, and on mathematical modelling of the temperature

410   window in which each mineral is likely to form (Butler et al., 2017; Marion et al., 2010).

411   There are still many uncertainties regarding the precipitation and dissolution of gypsum

412   within natural sea ice and during ice-core storage. Although the FREZCHEM model and

413   Gitterman Pathway predict gypsum precipitation under defined conditions, only Geilfus et al.

414   (Geilfus et al., 2013) and Butler et al. (Butler et al., 2017) succeeded in retrieving gypsum

415   under such conditions, whereas others failed (Butler and Kennedy, 2015). According to the

416   FREZCHEM model, cryogenic gypsum precipitates at temperatures of -6.2 to -8.5 °C and at

417   temperatures <-18 °C (Geilfus et al., 2013; Wollenburg et al., 2018a). Accordingly, a storage

418   temperature of -20 °C would allow the post-coring precipitation of gypsum from contained

419   brines. However, in field and experimental studies cryogenic gypsum was so far only

420   observed to precipitate in the -6.2 to -8.5 °C temperature window, even when treatments were

421   conducted below -20 °C (Butler et al., 2017; Geilfus et al., 2013). Furthermore, the observed

422   signs of dissolution on the large cryogenic gypsum crystals from the ice-core when compared

423   to the sharp-edged crystals retrieved from the water column at station 80 indicate that

424   significant new precipitation of gypsum during storage did not occur, rather the opposite.

425   Apart from the growing conditions of gypsum crystals within sea ice, the size spectrum of

426   crystals retrieved from different depths in the water column likely was essentially altered by

427   the size-dependent sinking velocity of the crystals. Because the sinking velocity of large

428   cryogenic gypsum crystals is high the chance to catch large crystals with horizontal transects

429   directly under the ice should be lower compared to small crystals (Fig. 7A). Accordingly,

430   significant amounts of large cryogenic gypsum crystals were mainly sampled from the 0 m

431   layer where they could be scraped off the underside of the ice (see station 66, Tab. 2). In

432   contrast, smaller cryogenic gypsum crystals sink at lower velocities (Fig. 7A). Hence, the

433   large quantity of small-sized crystals retrieved in the deeper layers of station 66, and all layers

434   of station 32 and 45 likely were influenced by the accumulated gypsum release in this size-

435   fraction, whereas the rarer large crystals indicated the momentary release at these stations.

436   The extremely large crystals sampled at station 80 at 10 m depth probably indicated an on-

437   going flux event during rapid melting. According to our dissolution experiments, gypsum

438   dissolution within Arctic surface waters should only have a minor impact on the size

439   distribution of cryogenic gypsum crystals within the surface water. Besides vertical flux,

440   advection of gypsum crystals with surface currents may also have influenced the size-

441   distribution of gypsum crystals sampled in the water column.

442

443   **4.2   Reasons why cryogenic gypsum was rarely observed in past studies**

444

445   The small temperature range of the -6.2 to -8.5 °C window, which is also the only gypsum

446   precipitation temperature spectrum applicable in the Arctic Ocean, has been considered one

447   reason why gypsum was not detected in other studies (Butler and Kennedy, 2015; Wollenburg

448   et al., 2018a). Furthermore, the kinetics of gypsum precipitation was considered as too slow

449   for detection during experimental studies, and the amount of gypsum hard to verify versus

450 other sea ice precipitates that are quantitatively much more abundant, leading the focus

451 towards other sea ice precipitates (Butler and Kennedy, 2015; Geilfus et al., 2013). Although

452 cryogenic mirabilite and hydrohalite are three and twenty-two times more abundant than

453 gypsum, respectively (Butler and Kennedy, 2015), gypsum is the only sea ice precipitate that

454 survives for one to several days within the Arctic water column. Cryogenic gypsum

455 dissolution increases with increasing hydrostatic pressure and increasing temperatures (Fig.

456 6). However, well-preserved cryogenic gypsum crystals were retrieved from algae aggregates

457 collected from 2,146 m water depth, suggesting that either the transport from the surface to

458 this depth was very rapid or that dissolution was decreased and/or prevented once gypsum

459 crystals were included within the matrix of organosulfur compound-rich aggregates

460 (Wollenburg et al., 2018a). Yet, as seawater is usually undersaturated with respect to gypsum

461 (Briskin and Schreiber, 1978a; Briskin and Schreiber, 1978b) and is shown by our dissolution

462 experiments, disaggregation of organic aggregates would expose the gypsum to the seawater

463 and dissolve any crystals making it to the deep ocean or seafloor likely within a few days. The

464 same dissolution would occur within the sampling cups of sediment traps, explaining why

465 gypsum has not been observed in those type of samples.

466 Our dissolution experiments showed that cryogenic gypsum can persist long enough in the

467 cold polar surface water to be collected in measurable concentrations. The missing evidence

468 of gypsum from past studies was likely due to the quick dissolution of gypsum crystals at

469 higher temperatures and pressure dependence of dissolution kinetics, impeding the discovery

470 of gypsum in sediment trap samples and on the sea-floor. In addition, Formaldehyde

471 preservation leads to the immediate dissolution of gypsum, destroying any evidence of

472 cryogenic gypsum in all kinds of biological samples including water column and net samples.

473 Based on our experience with the PS106 expedition samples and the experiments presented

474 here, we propose a standardized procedure for gypsum sampling in the field. This procedure

475 is part of the standard operating protocol for gypsum samplind on the MOSAIC expedition

476 (S 9).

477

478 **4.3   Potential of cryogenic gypsum as a ballast of algae blooms**

479

480 We found less than 6% dissolution of individual crystals in Polar Surface Water (PSW) per

481 day. Thus, at depths immediately below the fluorescence maximum where a significant part

482 of organic aggregates are formed (Iversen et al. 2010), the gypsum scavenging and ballasting

483 of aggregates (Turner, 2015) is little affected by gypsum dissolution (Olli et al., 2007) (Fig. 6,

484 Tab. 3). Incorporation of dense minerals into settling organic aggregates will increase their

485 density and, therefore, the size-specific sinking velocities of the aggregates (Iversen and

486 Ploug, 2010; Iversen and Robert, 2015; van der Jagt et al., 2018). The high sinking velocity of

487 large gypsum crystals >1 mm (5,000-7,000 m d^{-1} (Fig. 7A)) could create strong hydrodynamic

488 shear that might cause disaggregation of fragile algae aggregates (Olli et al., 2007). However,

489 smaller gypsum crystals have been observed inside *Phaeocystis* aggregates collected at depths

490 below 2000 m (Wollenburg et al. 2018a). This shows that cryogenic gypsum is incorporated

491 into organic aggregates and supports that gypsum can be an important ballast mineral of

492 organic aggregates.

493 As chlorophyll concentrations in the surface water were mostly low (< 1 mg m^{-3}, H.F.

494 unpublished data), a massive gypsum-mediated export of phytoplankton was unlikely during

495 expedition PS106. However, especially at the ice floe of station 32/80, we observed a high

496 coverage of the ice underside by the filamentous algae *Melosira arctica*, and gypsum crystals

497 were found in *M. arctica* filaments collected nearby (Fig. 8) as well as at station 45 (Fig. 2D).

498 This indicates a potential for rapid *M. arctica* downfall mediated by cryogenic gypsum, as

499 soon as the algal filaments were released from the melting sea ice. Hence, ballasting by

500 cryogenic gypsum may also have contributed to the mass export of *Melosira arctica*

501 aggregates observed in 2012 (Boetius et al. 2013).

502

503

504

505 **5   Conclusions**

506 This study shows for the first time that gypsum released to the water at the onset of melt

507 season in the Arctic Ocean causes a constant flux of gypsum over wide spread areas and over

508 a long period of time (> six weeks). The morphological diversity of gypsum crystals retrieved

509 from Arctic surface waters and ice-cores indicated a complex variety of precipitation and

510 release processes as well as modifications during sea ice formation, the melt phase, and in the

511 water column. In the fresh and cold Polar surface water, gypsum crystals persist long enough

512 to act as an effective ballast on organic matter, such as phytoplankton filaments and marine

513 snow.

514

515 **References:**

516 Arrigo, K. R., Perovich, D. K., Pickart, R. S., Brown, Z. W., van Dijken, G. L., Lowry, K. E., Mills,
517 M. M., Palmer, M. A., Balch, W. M., Bahr, F., Bates, N. R., Benitez-Nelson, C., Bowler, B.,
518 Brownlee, E., Ehn, J. K., Frey, K. E., Garley, R., Laney, S. R., Lubelczyk, L., Mathis, J., Matsuoka,

A., Mitchell, B. G., Moore, G. W. K., Ortega-Retuerta, E., Pal, S., Polashenski, C. M., Reynolds, R. A., Schieber, B., Sosik, H. M., Stephens, M., and Swift, J. H.: Massive Phytoplankton Blooms Under Arctic Sea Ice, Science, 336, 1408, 2012.

Arrigo, K. R., Perovich, D. K., Pickart, R. S., Brown, Z. W., van Dijken, G. L., Lowry, K. E., Mills, M. M., Palmer, M. A., Balch, W. M., Bates, N. R., Benitez-Nelson, C. R., Brownlee, E., Frey, K. E., Laney, S. R., Mathis, J., Matsuoka, A., Greg Mitchell, B., Moore, G. W. K., Reynolds, R. A., Sosik, H. M., and Swift, J. H.: Phytoplankton blooms beneath the sea ice in the Chukchi sea, Deep Sea Research Part II: Topical Studies in Oceanography, 105, 1-16, 2014.

Assmy, P., Fernández-Méndez, M., Duarte, P., Meyer, A., Randelhoff, A., Mundy, C. J., Olsen, L. M., Kauko, H. M., Bailey, A., Chierici, M., Cohen, L., Doulgeris, A. P., Ehn, J. K., Fransson, A., Gerland, S., Hop, H., Hudson, S. R., Hughes, N., Itkin, P., Johnsen, G., King, J. A., Koch, B. P., Koenig, Z., Kwasniewski, S., Laney, S. R., Nicolaus, M., Pavlov, A. K., Polashenski, C. M., Provost, C., Rösel, A., Sandbu, M., Spreen, G., Smedsrud, L. H., Sundfjord, A., Taskjelle, T., Tatarek, A., Wiktor, J., Wagner, P. M., Wold, A., Steen, H., and Granskog, M. A.: Leads in Arctic pack ice enable early phytoplankton blooms below snow-covered sea ice, Scientific Reports, 7, 40850, 2017.

Briskin, M. and Schreiber, B. C.: Authigenic gypsum in marine sediments, Marine Geology, 28, 37-49, 1978.

Butler, B.: Mineral dynamics in sea ice brines, PhD, Bangor, 184 pp., 2016.

Butler, B. M. and Kennedy, H.: An investigation of mineral dynamics in frozen seawater brines by direct measurement with synchrotron X-ray powder diffraction, Journal of Geophysical Research: Oceans, 120, 5686-5697, 2015.

Butler, B. M., Papadimitriou, S., Day, S. J., and Kennedy, H.: Gypsum and hydrohalite dynamics in sea ice brines, Geochimica et Cosmochimica Acta, 213, 17-34, 2017.
Culberson, C. and Pytkowicx, R. M.: Effect of pressure on carbonic acid, boric acid, and the pH in seawater, Limnology and Oceanography, 13, 403-417, 1968.

Damm, E., Bauch, D., Krumpen, T., Rabe, B., Korhonen, M., Vinogradova, E., and Uhlig, C.: The Transpolar Drift conveys methane from the Siberian Shelf to the central Arctic Ocean, Scientific Reports, 8, 4515, 2018.

Docquier, D., Massonnet, F., Barthélemy, A., Tandon, N. F., Lecomte, O., and Fichefet, T.: Relationships between Arctic sea ice drift and strength modelled by NEMO-LIM3.6, The Cryosphere, 11, 2829-2846, 2017.

Edler, L.: Recommendations on Methods for Marine Biological Studies in the Baltic Sea: Phytoplankton and chlorophyll, Department of Marine Botany, University of Lund, 1979.
Flores, H. E., J.; Lange, B.; Sulanke, E.; Niehoff, B.; Hildebrandt, N.; Doble, M.; Schaafsma, F.; Meijboom, A.; Fey, B.; Kühn, S.; Bravo-Rebolledo; E.; Dorssen, M. van; Grandinger, R.; Hasset, B.; Kunisch, E.; Kohlbach, D.; Graeve, M.; Franeker, J. A. van; Gradinger, Bluhm, B.: Under-ice fauna, zooplankton and endotherms. In: The Expeditions PS106/1 and 2 of the

Research Vessel Polarstern to the Arctic Ocean in 2017, Macke, A. F., H. (Ed.), Reports on polar and marine research, 2018.

Geilfus, N. X., Galley, R. J., Cooper, M., Halden, N., Hare, A., Wang, F., Søgaard, D. H., and Rysgaard, S.: Gypsum crystals observed in experimental and natural sea ice, Geophysical Research Letters, 40, 6362-6367, 2013.

Girard-Ardhuin, F. and Ezraty, R.: Enhanced Arctic Sea Ice Drift Estimation Merging Radiometer and Scatterometer Data, IEEE Transactions on Geoscience and Remote Sensing, 50, 2639-2648, 2012.

Golden, K. M., Ackley, S. F., and Lytle, V. I.: The Percolation Phase Transition in Sea Ice, Science, 282, 2238, 1998.

Iversen, M., Nowald, N., Ploug, H., A. Jackson, G., and Fischer, G.: High resolution profiles of vertical particulate organic matter export off Cape Blanc, Mauritania: Degradation processes and ballasting effects, Deep Sea Research Part I Oceanographic Research Papers, 57, 771-784, 2010.

Iversen, M. H. and Ploug, H.: Ballast minerals and the sinking carbon flux in the ocean: carbon-specific respiration rates and sinking velocity of marine snow aggregates, Biogeosciences, 7, 2613-2624, 2010.

Iversen, M. H. and Robert, M. L.: Ballasting effects of smectite on aggregate formation and export from a natural plankton community, Marine Chemistry, 175, 18-27, 2015.
Katlein, C., Arndt, S., Nicolaus, M., Perovich, D. K., Jakuba, M. V., Suman, S., Elliott, S., Whitcomb, L. L., McFarland, C. J., Gerdes, R., Boetius, A., and German, C. R.: Influence of ice thickness and surface properties on light transmission through Arctic sea ice, Journal of Geophysical Research: Oceans, 120, 5932-5944, 2015.

Katlein, C., Nicolaus, M., Sommerfeld, A., Copalorado, V., Tiemann, L., Zanatta, M., Schulz, H., and Lange, B.: Sea Ice Physics. In: The Expeditions PS106/1 and 2 of the research vessel Polarstern in the Arctic Ocean in 2017, Macke, A. F., H. (Ed.), Berichte zur Polarforschung Bremerhaven, 2018.

Katlein, C., Schiller, M., Belter, H. J., Coppolaro, V., Wenslandt, D., and Nicolaus, M.: A New Remotely Operated Sensor Platform for Interdisciplinary Observations under Sea Ice, Frontiers in Marine Science, 4, 281, 2017.

Krumpen, T.: AWI ICETrack - Antarctic and Arctic Sea Ice Monitoring and Tracking Tool Alfred-Wegener-Institut Hemholtz-Zentrum für Polar- und Meeresforschung, Bremerhaven, Germany, 2018.

Krumpen, T., Belter, H. J., Boetius, A., Damm, E., Haas, C., Hendricks, S., Nicolaus, M., Nöthig, E.-M., Paul, S., Peeken, I., Ricker, R., and Stein, R.: Arctic warming interrupts the Transpolar Drift and affects long-range transport of sea ice and ice-rafted matter, Scientific Reports, 9, 5459, 2019.

Krumpen, T., Gerdes, R., Haas, C., Hendricks, S., Herber, A., Selyuzhenok, V., Smedsrud, L., and Spreen, G.: Recent summer sea ice thickness surveys in Fram Strait and associated ice volume fluxes, The Cryosphere, 10, 523-534, 2016.

Kwok, R.: Arctic sea ice thickness, volume, and multiyear ice coverage: losses and coupled variability (1958–2018), Environmental Research Letters, 13, 105005, 2018.

Kwok, R. and Rothrock, D. A.: Decline in Arctic sea ice thickness from submarine and ICESat records: 1958‚Äì2008, Geophys. Res. Lett., 36, 2009.
Lavergne, T.: Validation and Monitoring of the OSI SAF Low Resolution Sea Ice Drift Product (v5), 2016.

Lieb-Lappen, R. M., Golden, E. J., and Obbard, R. W.: Metrics for interpreting the microstructure of sea ice using X-ray micro-computed tomography, Cold Regions Science and Technology, 138, 24-35, 2017.

Marion, G. M., Mironenko, M. V., and Roberts, M. W.: FREZCHEM: A geochemical model for cold aqueous solutions, Computers & Geosciences, 36, 10-15, 2010.

Nicolaus, M., Arndt, S., Katlein, C., Maslanik, J., and Hendricks, S.: Correction to "Changes in Arctic sea ice result in increasing light transmittance and absorption", Geophysical Research Letters, 40, 2699-2700, 2013.

Nicolaus, M., Katlein, C., Maslanik, J., and Hendricks, S.: Changes in Arctic sea ice result in increasing light transmittance and absorption, Geophysical Research Letters, 39, 2012.

Nikolopoulos, A., Heuzé, C., Linders, T., Andrée, E., and Sahlin, S.: Physical Oceanography. In: The Expeditions PS106/1 and 2 of the Research Vessel POLARSTERN to the Arctic Ocean in 2017, Macke, A. and Flores, H. (Eds.), Reports on Polar and Marine Research, Alfred-Wegener Institute Helmholtz Centre for Polar and marine research, Bremerhaven, 2018.

Nürnberg, D., Wollenburg, I., Dethleff, D., Eicken, H., Kassens, H., Letzig, T., Reimnitz, E., and Thiede, J.: Sediments in Arctic sea ice: Implications for entrainment, transport and release, Marine Geology, 119, 185-214, 1994.

Olli, K., Wassmann, P., Reigstad, M., Ratkova, T. N., Arashkevich, E., Pasternak, A., Matrai, P. A., Knulst, J., Tranvik, L., Klais, R., and Jacobsen, A.: The fate of production in the central Arctic Ocean - top-down regulation by zooplankton expatriates?, Progress In Oceanography, 72, 84-113, 2007.

Peeken, I., Primpke, S., Beyer, B., Gütermann, J., Katlein, C., Krumpen, T., Bergmann, M., Hehemann, L., and Gerdts, G.: Arctic sea ice is an important temporal sink and means of transport for microplastic, Nature Communications, 9, 1505, 2018.

Peeken, I. C., G.; Flores, H.; Ehrlich, J.; Lange, B.; Schaafsma, F., Gradinger, R.; Hassett, B.; Kunisch, E.; Damm, E.; Verdugo, J.; Kohlbach, D.; Graeve, M.; Bluhm, B.: Sea ice biology and biogeochemistry. In: The Expeditions PS106/1 and 2 of the Research Vessel Polarstern to the Arctic Ocean in 2017, Macke, A. F., H. (Ed.), 719, Reports of polar and marine research, 2018.

661 Ploug, H., Iversen, M. H., Koski, M., and Buitenhuis, E. T.: Production, oxygen respiration
662 rates, and sinking velocity of copepod fecal pellets: Direct measurements of ballasting by
663 opal and calcite, Limnology and Oceanography, 53, 469-476, 2008.
664
665 Rudels, B.: Arctic Ocean circulation, processes and water masses: A description of
666 observations and ideas with focus on the period prior to the International Polar Year 2007–
667 2009, Progress in Oceanography, 132, 22-67, 2015.
668
669 Schneider, C. A., Rasband, W. S., and Eliceiri, K. W.: NIH Image to ImageJ: 25 years of image
670 analysis, Nature Methods, 9, 671, 2012.
671
672 Smedsrud, L. H., Halvorsen, M. H., Stroeve, J. C., Zhang, R., and Kloster, K.: Fram Strait sea ice
673 export variability and September Arctic sea ice extent over the last 80 years, The Cryosphere,
674 11, 65-79, 2017.
675
676 Strunz, H. and Nickel, E. H.: Strunz Mineralogical Tables. Chemical-structural Mineral
677 Classification System, Schweizerbart'sche Verlagsbuchhandlung (Nägele u. Obermiller),
678 Stuttgart, 2001.
679
680 Tschudi, S., Fowler, C., Maslanik, J., Stewart, J., and Stewart, W.: Polar Pathfinder Daily 25 km
681 EASE-Grid Sea Ice Motion Vectors. In: Technical report, NASA National Snow and Ice Data
682 Center Distributed Active Archive Center, Boulder, Colorado USA 2016.
683
684 Turner, J. T.: Zooplankton fecal pellets, marine snow, phytodetritus and the ocean's
685 biological pump, Progress in Oceanography, 130, 205-248, 2015.
686
687 van der Jagt, H., Friese, C., Stuut, J.-B. W., Fischer, G., and Iversen, M. H.: The ballasting
688 effect of Saharan dust deposition on aggregate dynamics and carbon export: Aggregation,
689 settling, and scavenging potential of marine snow, Limnology and Oceanography, 63, 1386-
690 1394, 2018.
691
692 Weissenberger, J., Dieckmann, G., Gradinger, R., and Spindler, M.: Sea ice: A cast technique
693 to examine and analyze brine pockets and channel structure, Limnology and Oceanography,
694 37, 179-183, 1992.
695
696 Wollenburg, J. E., Katlein, C., Nehrke, G., Nöthig, E. M., Matthiessen, J., Wolf- Gladrow, D. A.,
697 Nikolopoulos, A., Gázquez-Sanchez, F., Rossmann, L., Assmy, P., Babin, M., Bruyant, F.,
698 Beaulieu, M., Dybwad, C., and Peeken, I.: Ballasting by cryogenic gypsum enhances carbon
699 export in a Phaeocystis under-ice bloom, Scientific Reports, 8, 7703, 2018a.
700
701 Wollenburg, J. E., Zittier, Z. M. C., and Bijma, J.: Insight into deep-sea life – Cibicidoides
702 pachyderma substrate and pH-dependent behaviour following disturbance, Deep Sea
703 Research Part I: Oceanographic Research Papers, 138, 34-45, 2018b.
704

705

706

707 **Table captions:**

708

709 Tab. 1: Properties of sea ice stations and characteristics of ROVnet profiles.

Cruise Site	Date	Latitude (Deg N)	Longitude (Deg E)	Ocean depth (m)	Sampling depth	Water temp. (°C)	Salinity	Mean ice thickness (m)	Filtered water volume (m³)
PS106.1 Stat. 32	2017-06-15	81.73	10.86	1608	under-ice	-1.94	34.27	1.90	2.2
					5 m	n.a	n.a.	1.90	3.9
PS106.2 Stat. 45	2017-06-25	78.10	30.47	233	under-ice	-1.52	33.84	1.00	2.3
					5 m	-1.47	34.11	1.00	4.5
					10 m	-1.68	34.29	1.00	2.5
PS106.2 Stat. 66	2017-07-02	81.66	32.34	1506	under-ice	-1.67	33.18	1.80	3.1
					5 m	-1.71	33.76	1.80	2.7
					10 m	-1.73	33.78	1.80	3.1
PS106.2 Stat. 80	2017-07-12	81.37	17.13	1010	10 m	-1.37	32.87	1.80	1.7

710
711

712   Tab. 2: Size measurements and percentage of mass contribution of gypsum crystals from the

713   >63 μm size fraction and the >30 < 63 μm size fraction

Cruise, Site, mean water depth of the catch	>63 µm fraction			>30<63 µm fraction			>63 µm fraction weight%	>30<63 µm fraction weight%
	Mean length µm	Mean width µm	length/ width ratio	Mean length µm	Mean width µm	length/ width ratio		
PS106.1, Stat. 32, 0 m	68.46	44.27	1.55	50.64	35.03	1.45	43.70	56.30
PS106.1, Stat. 32, 5 m	63.28	35.90	1.76	49.91	35.57	1.40	33.72	66.28
PS106.1, Stat. 32, mean (0-5 m)	65.87	40.09	1.64	50.28	35.30	1.42	38.71	61.29
PS106.2, Stat. 45, 0 m	114.18	65.93	1.73	58.74	42.84	1.37	79.90	20.10
PS106.2, Stat. 45, 5 m	110.98	64.84	1.71	56.73	38.89	1.46	73.39	26.61
PS106.2, Stat. 45 , 10 m	92.83	46.81	1.98	50.32	29.98	1.68	66.14	33.86
PS106.2, Stat. 45 , mean (0-10 m)	85.49	44.45	1.92	77.93	24.28	3.21	73.14	26.86
PS106.2, Stat. 66, 0 m	1355.38	415.10	3.27	56.67	25.63	2.21	99.25	0.75
PS106.2, Stat. 66, 5 m	411.42	73.45	5.60	62.03	12.20	5.08	75.23	24.77
PS106.2, Stat. 66, 10 m	101.40	23.19	4.37	30.71	5.79	5.30	61.18	38.82
PS106.2, Stat. 66, mean (0-10 m)	599.17	164.78	3.64	59.96	12.61	4.76	58.16	41.84
PS106.2, Stat. 80, 10 m	3078.44	1830.00	1.68	71.78	30.76	2.33	89.05	10.95

714

715

716

717   Tab. 3: Dissolution experiments on cryogenic gypsum crystals. 'Water mass' simulating

718   experiments with 34.9‰ sterile filtered seawater. Each experiment was conducted in parallel

719   in 3-4 separate pressure chambers.

Chamber (no.)/Water mass	Dissolution in weight%				
	PSW	AW	EADW (1)	EADW (2)	EADW (3)
1	11.34	76.22	47.52	57.08	74.92
2	1.33	86.23	26.09	71.03	53.77
3	8.29	82.93	21.05	47.15	57.43
4	2.99	78.57	10.91	58.56	
Mean	5.99	80.77	26.39	58.34	62.04

720

721

Figure captions:
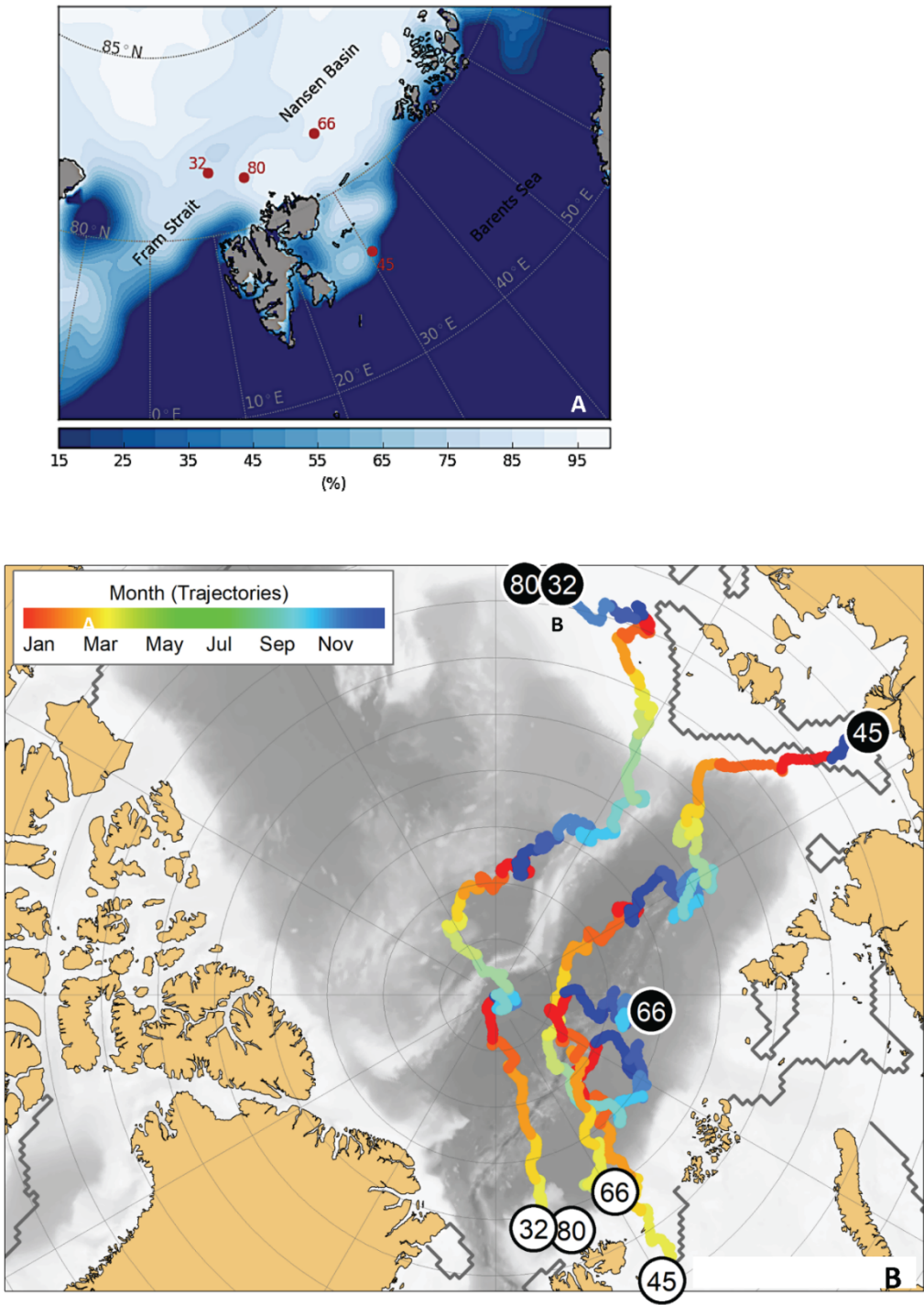
Fig. 1:

Study area with sample locations. A: Sea ice coverage at the station and time of sampling in %. B) Trajectories of the sea ice from which the cryogenic gypsum was released. Each trajectory starts where sea ice formed (black circles), and shows its drift until the time and place of sampling (white circles). The colour scale of the drift trajectories indicates the month in which the back-tracked sea ice was at any given position.

730
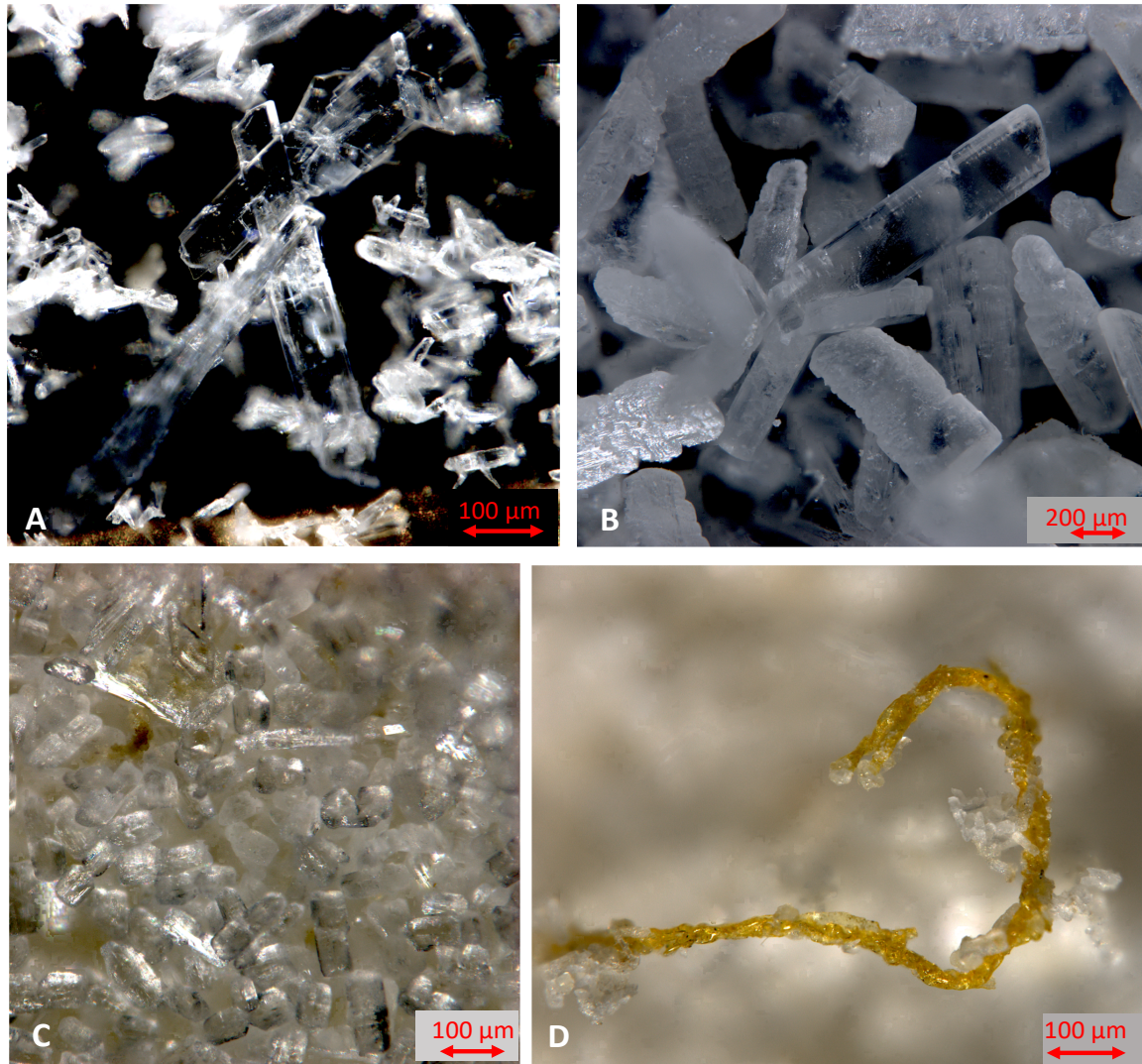
731 Fig. 2: Cryogenic gypsum crystals collected during Polarstern expedition PS106-1 from the

732 upper water column. A) Crystals collected from station 66 at 5 m water depth. B) Crystals

733 collected from station 66 at 0 m water depths. C) Crystals collected from station 45 at 10 m

734 water depth. D) Crystals collected from station 45 at 10 m water depths entangled in an algae

735 filament.

736

737

738

739
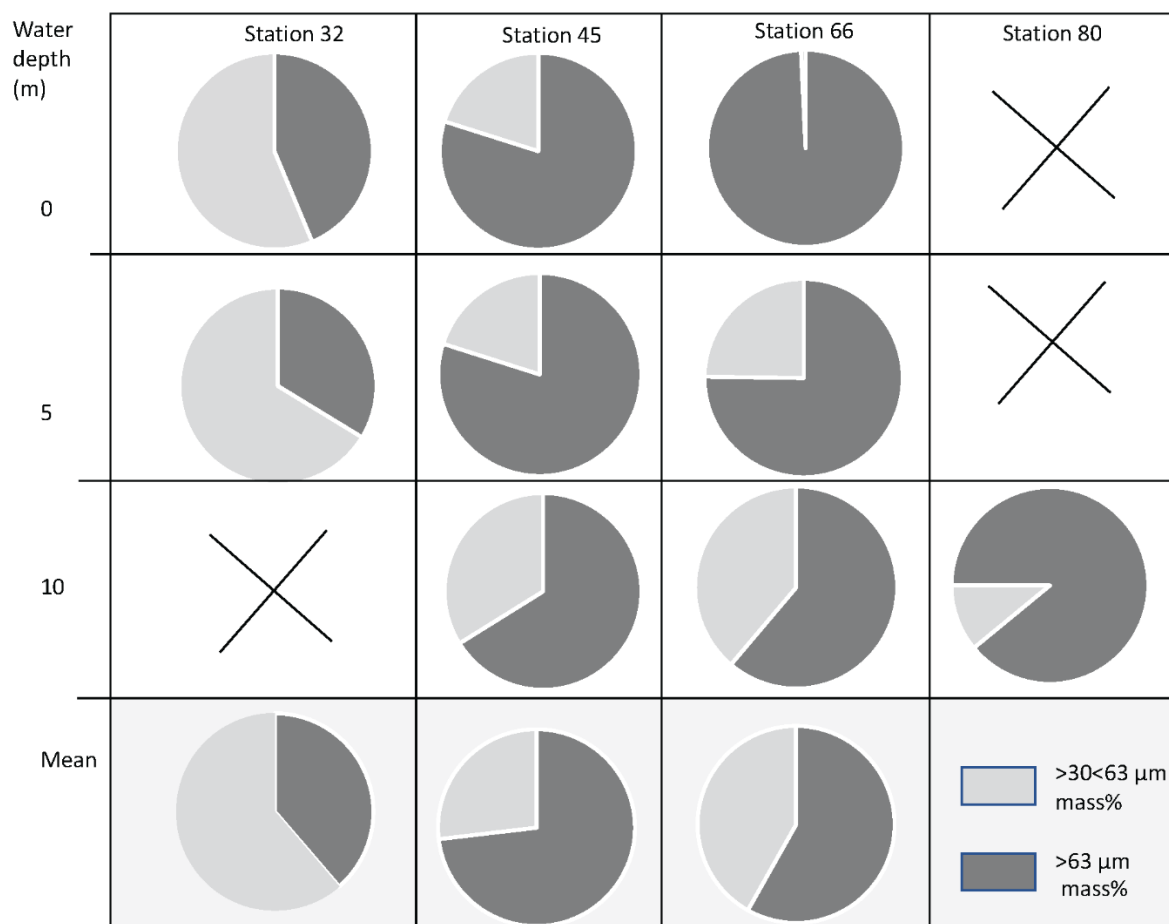
740 Fig. 3: Proportional mass (%) of cryogenic gypsum for the size fractions >30<63 μm and >63

741 μm for all ROV samples.

742
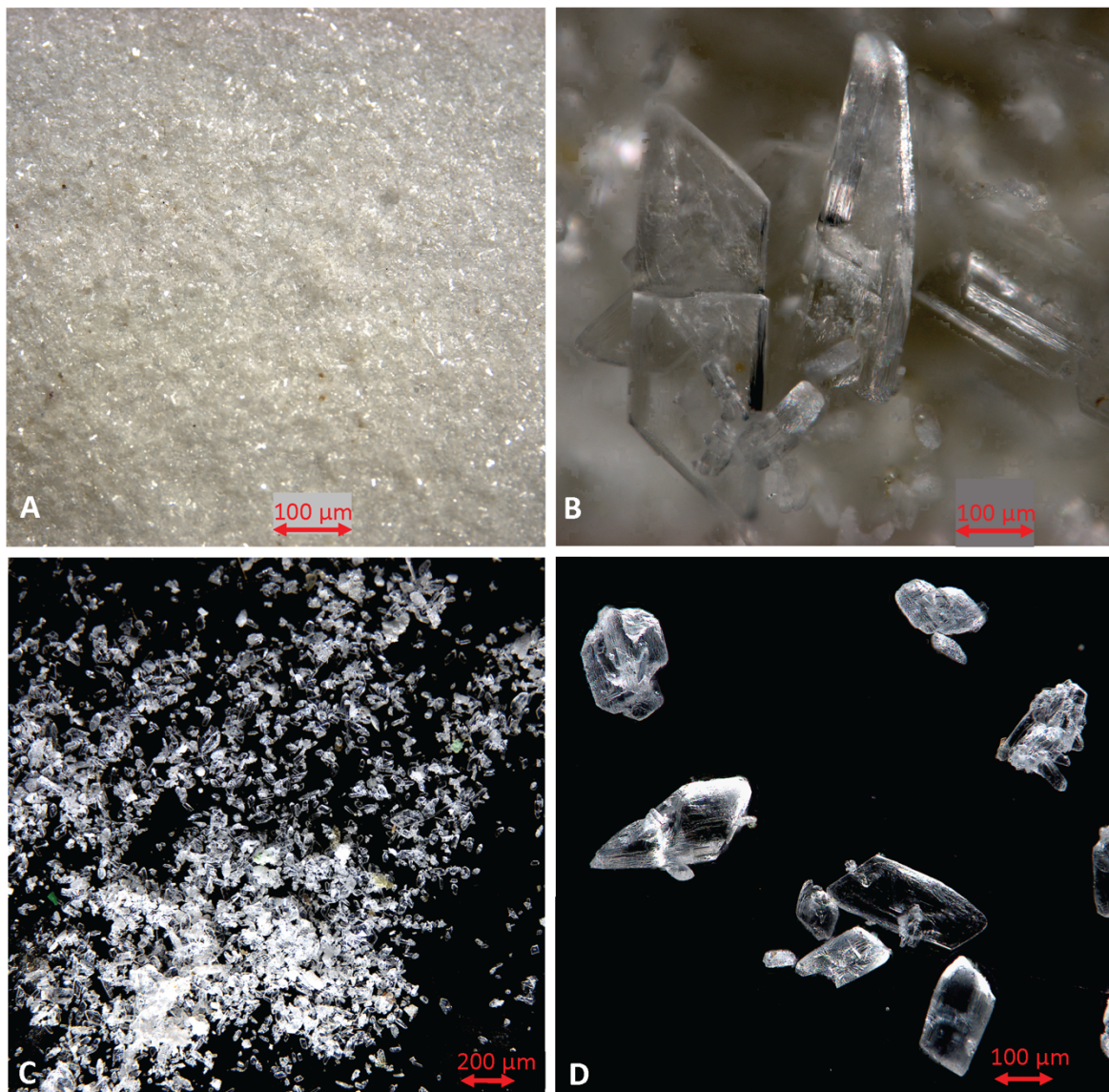
Fig. 4: Comparison of cryogenic gypsum crystals collected from the water column at station PS45 (10 m water depth) (A-B) with crystals retrieved from an ice-core collected above the ROVnet sampling area (C-D).

749
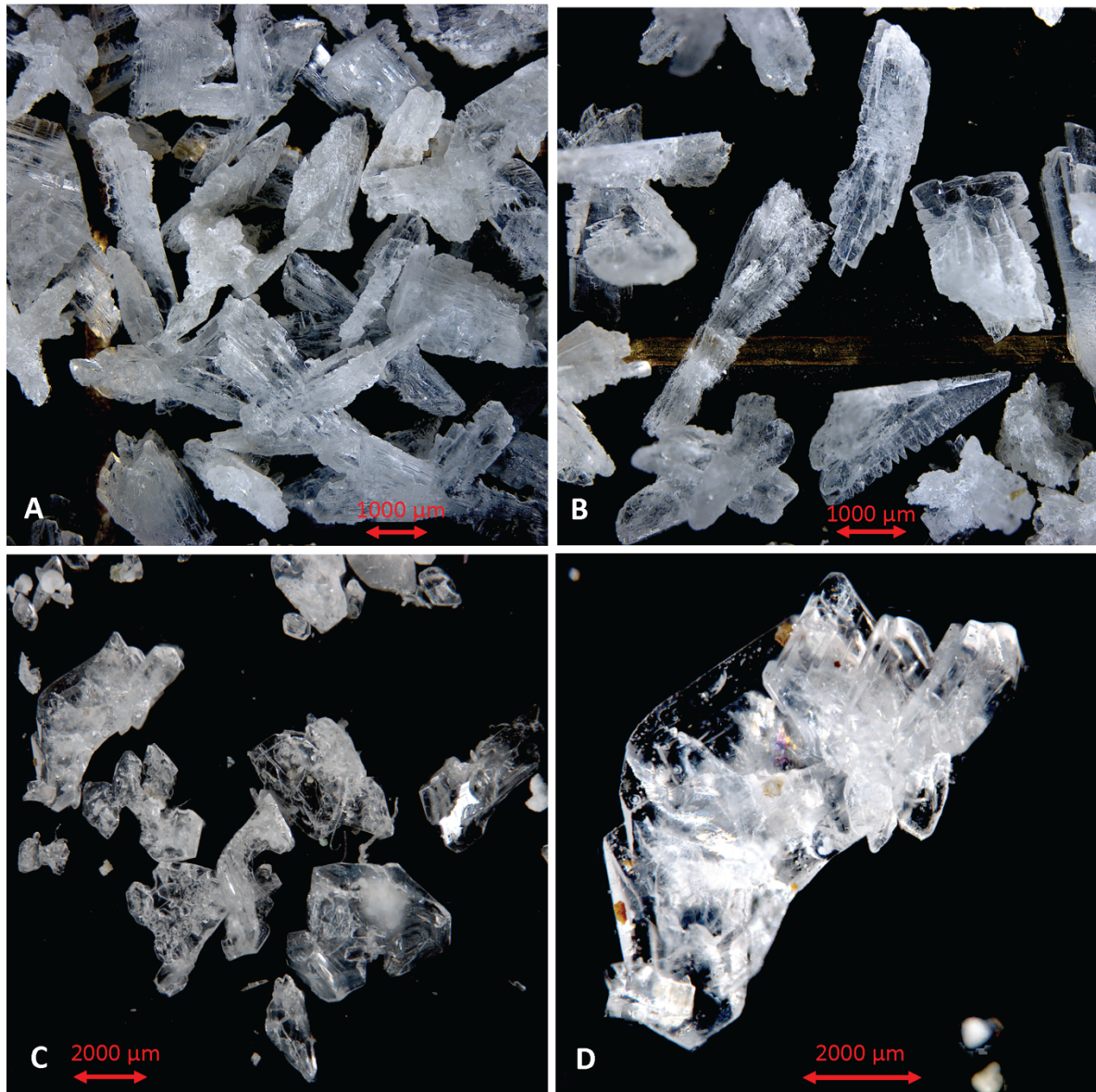
750 Fig. 5: Comparison of cryogenic gypsum crystals collected from the water column at station

751 PS80-2 (10 m water depth) (A-B) with crystals retrieved from an ice-core collected above the

752 ROVnet sampling area (C-D).

753

754

755
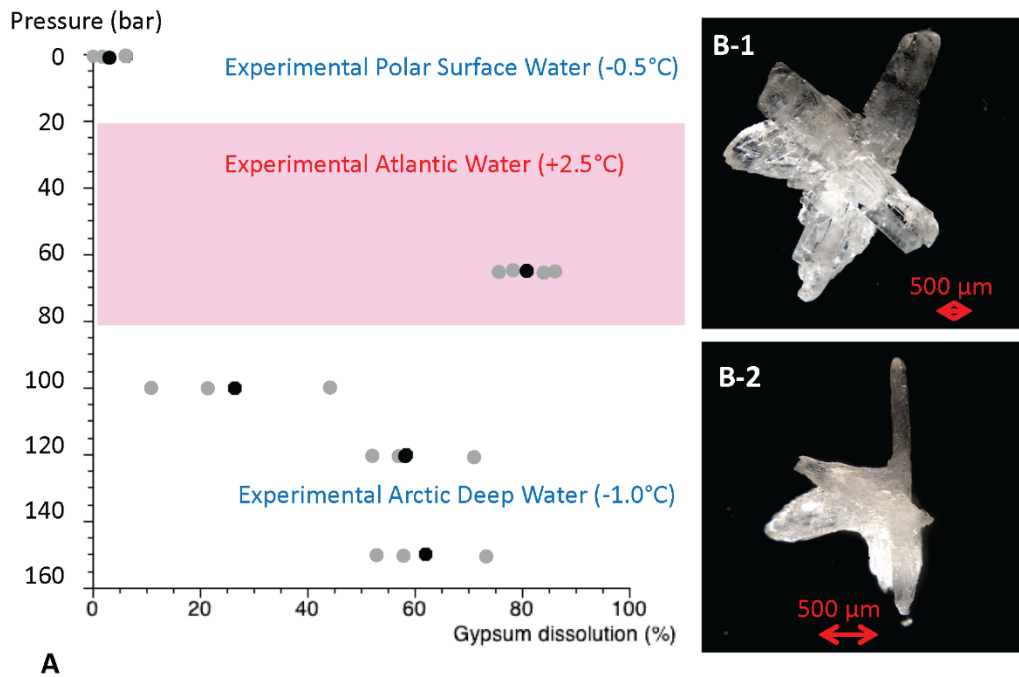
756 Figure 6: Results from cryogenic gypsum dissolution experiments. A) Graph showing the

757 position of the simulated Arctic water masses in respect to pressure and temperature and how

758 much gypsum (%) was dissolved on average over a 24-hours lasting exposure to such

759 pressure and temperature conditions. Grey dots indicate the values from each aquarium, black

760 dots the mean per experiment. B-1) Cryogenic gypsum crystal of the 120 bar-experiment

761 before exposure. B-2) The same cryogenic gypsum crystal of the 120 bar-experiment after 24

762 hours.

763

764

765
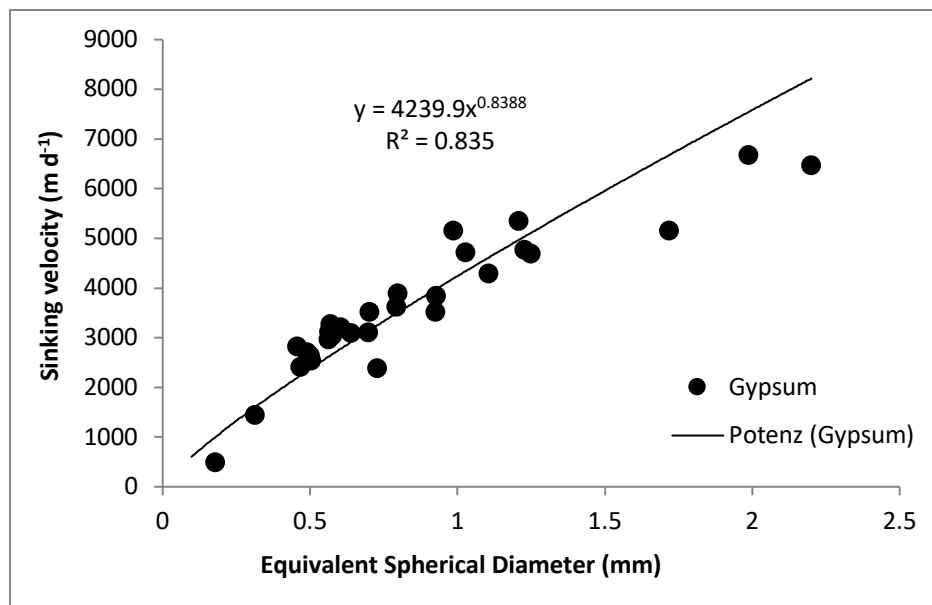
766 Fig. 7: Sinking velocity of cryogenic gypsum crystals plotted against equivalent spherical

767 diameter (ESD).

768

769
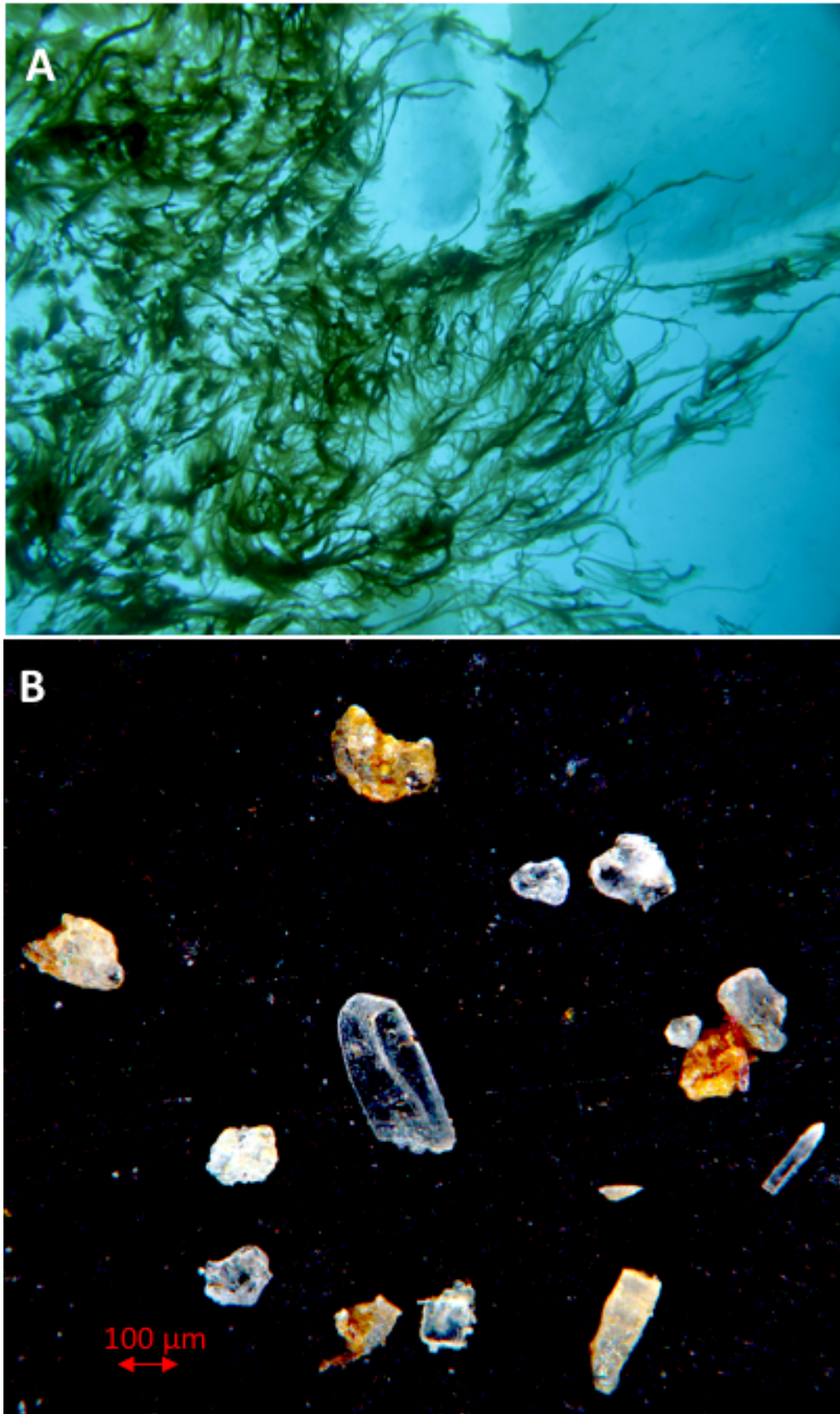
Fig. 8: Living *Melosira arctica* curtains hanging from ice flows during the PS106 expedition

(photo taken by M. Nicolaus and C. Katlein). Cryogenic gypsum isolated from *Melosira*

arctica (PS106-1, station 21(Peeken, 2018)).

773

774

Acknowledgement:

We thank Gernot Nehrke for performing Raman Spectroscopy on crystals from all catches. Christoph Vogt and Dieter Wolf-Gladrow made valuable comments on the manuscript. We thank the captain and crew of RV Polarstern expedition PS106 for their support at sea. This study was funded by the PACES (Polar Regions and Coasts in a Changing Earth System) Program of the Helmholtz Association, the Helmholtz Infrastructure Fund "Frontiers in Arctic Marine Monitoring (FRAM)". This study used samples and data provided by the Alfred-Wegener-Institut Helmholtz-Zentrum für Polar- und Meeresforschung in Bremerhaven from *Polarstern* expedition PS 106 (Grant No. AWI-PS106_00).

Author Contributions:

J.W., H.F: and M.I. designed this study. J.W. lead the writing of this manuscript and performed gypsum sample preparation and analysis. H.F., I.P., C.K., G.C., M.N. acquired ROVnet and ice samples in the field. M.I. measured crystal settling velocities. T.K. performed the backtracking analysis. All authors contributed to the writing and editing of the manuscript